



TECHNICAL ARTICLE

The Temperature-Dependent Phase Transformation and Microstructural Characterisation in In-Sn Solder Alloys

JIYE ZHOU,¹ XIN FU TAN ^{1,2,4} QINFEN GU,³ STUART D. MCDONALD,¹ and KAZUHIRO NOGITA¹

1.—School of Mechanical and Mining Engineering, The University of Queensland, St. Lucia, QLD 4072, Australia. 2.—Department of Applied Quantum Physics and Nuclear Engineering, Kyushu University, Fukuoka 819-0395, Japan. 3.—Australian Synchrotron, ANSTO, Clayton, VIC 3168, Australia. 4.—e-mail: xin.tan@uq.edu.au

Indium-based solder alloys are considered candidates for the next generation of low-temperature solder materials, especially for superconducting joints because of the properties of the β -In₃Sn phase. The temperature-dependent phase transformation and thermal expansion behaviour of two different solder compositions including In-35Sn (in wt.%) and In-25.6Sn have been characterised using an in situ synchrotron powder X-ray diffraction method. The *c*-axis of the β -In₃Sn unit cell in the In-35Sn alloy exhibited a complex relationship with increasing temperature compared to the positive increasing trend in In-25.6Sn due to the temperature-dependent solubility of Sn in β -In₃Sn and change in the volume fraction of phases commencing at 80°C. In situ heating scanning electron microscopy recorded a real-time melting-solidification microstructure variation and phase transition during annealing at 90°C that was further analysed using energy dispersive X-ray spectroscopy. The observations are discussed with respect to the lattice parameters of the γ -InSn₄ and β -In₃Sn phases and the proportions and composition of both phases present within the alloys.

INTRODUCTION

With the diversification and miniaturisation of electronic devices, developing more reliable solder joints to meet different design requirements is an industry priority. It has been reported that the coefficient of thermal expansion (CTE) is a factor closely related to the reliability of electrical joints as the difference between the CTE of solders and substrates results in a poor resistance to thermal fatigue which occurs in electronic devices during operation.^{1–4} Furthermore, it has been proven that the life cycle and reliability of electronic devices are significantly influenced by the temperature as the cracks induced by thermal stress can cause failure in electrical joints.^{5,6} For instance, central processing units (CPUs) in computers can easily go up to 80°C during operation, and such temperature

excursions can result in phase transformations in the microstructure which significantly decrease the reliability of solder joints.^{3,7,8}

Meanwhile, low temperature lead-free solder alloys have received much attention over the years to meet greenhouse gas (GHG) emission reduction targets for electronics manufacturing. In-Sn alloys are possible next-generation low-temperature lead-free solders especially for flexible circuit, flip chip on flex (FCOF)⁹ and cryogenic applications due to their good ductility, lower melting point and ability to react with copper substrates.^{10–13} Moreover, indium-based solder alloys are considered promising candidates for electrical joints in space exploration because of their good ductility and electrical conductivity under large temperature fluctuations (e.g., –90°C to +20°C during Martian night and day).¹³

Among a wide range of compositions in the In-Sn binary system, In-35Sn (in wt.%) has been studied as it has superconductivity facilitated by a combination of two different phases, β -In₃Sn and γ -InSn₄,

(Received November 30, 2022; accepted April 20, 2023; published online May 16, 2023)

in the microstructure at room temperature.^{14,15} It has been reported that β -In₃Sn is a superconducting phase which has a body-centred tetragonal crystalline structure (space group I4/mmm, $a = 3.4715 \text{ \AA}$, $c = 4.3869 \text{ \AA}$) (PDF 04-002-9972), while γ -InSn₄ has a hexagonal crystalline structure (space group P6/mmm, $a = 3.2159 \text{ \AA}$, $c = 2.9972 \text{ \AA}$) (PDF 00-048-1547). The change in volume fraction between the two phases in the microstructure has been proven to be a time-temperature-dependent process and closely associated with the properties of solder joints.^{15,16}

Several studies revealed that the strong anisotropic thermal expansion of tetragonal β -Sn (space group I4₁/amd, $a = 5.83230 \text{ \AA}$, $c = 3.18230 \text{ \AA}$) (COD 7040217) in common Pb-free solders leads to a CTE mismatch and can induce cracks in intermetallic compounds (IMCs).^{6,17-19} The tetragonal and hexagonal crystal structures of β -In₃Sn and γ -InSn₄ are also anisotropic, and the phase transformation in the microstructure is critical to the performance; thus, it is worth investigating the temperature-dependent properties in In-Sn alloys and characterising the CTE and volume fraction variation of In-Sn solder alloys with respect to their potential reliability in different temperature regimes. This study uses a combination of variable temperature synchrotron-based powder X-ray diffraction (PXRD), differential scanning calorimetry (DSC) and in situ heating scanning electron microscopy (SEM) supported by energy-dispersive X-ray spectroscopy (EDX) to examine the temperature-dependant changes that occur in two In-Sn based alloys.

MATERIALS AND METHODS

Raw Sample Preparation

Two compositions, In-35Sn and In-25.6Sn, were selected for this study. The In-25.6Sn is a reference as it has a 100% β -In₃Sn in the microstructure compared to In-35Sn, which contains both β -In₃Sn and γ -InSn₄ (see the equilibrium phase diagram in Fig. 1). The corresponding proportions of pure indium (99.995%) ingots (supplied by Nihon Superior Co., Ltd., Japan) and tin (99.99%) ingots (supplied by Northern Smelters Pty. Ltd., Australia) were alloyed to obtain the In-25.6Sn and In-35Sn bulk samples. Ingots were melted in a boron-nitride-coated ceramic crucible at 300°C in a laboratory oven for 1 h with stirring at 15-min intervals to achieve a homogeneous structure. Dross on the surface was removed before cooling.

In Situ Synchrotron Powder X-ray Diffraction

As the indium-based alloys were too ductile to be crushed into fine powder in an agate mortar (normal XRD sample preparation method), a new method has been developed to fit samples in the capillary. As shown in Fig. 1a, samples were melted at 200°C, which is above their equilibrium melting point on a

hot plate; a small vacuum pump was used to suck the liquid sample into a 500- μm -diameter quartz capillary that was connected to the pump by a plastic tube and pipette as adaptor.

The in situ heating PXRD experiments were performed at the powder diffraction beamline of the Australian Synchrotron. The capillary was fitted on a rotary holder and heated to 150°C (above the samples' melting points) by a hot air blower. The PXRD experiments were performed using a 21-keV monochromatic incident beam under a ramp rate of 30°C/min. PXRD patterns for both samples were obtained every 10°C from 30°C to 150°C under atmospheric pressure. As shown in Fig. 2b, 2-min scans were performed (1 min at each Mythen strip detector position), for a total of 6 min (3 scans) of data collection at each temperature up to the maximum of 150°C, before directly cooling to 30°C. The obtained PXRD patterns were post-processed by PDViPeR software, and Rietveld refinement performed by TOPAS V6 software (Bruker-AXS, Germany) was used to characterise the lattice parameters in crystal structure (see Fig. 2c). The X-ray beam was calibrated by a standard LaB₆ sample (NIST660b, $a = 4.15689 \text{ \AA}$, cubic, Pm-3 m), which gave a wavelength of 0.5908 Å.

Characterisation of Thermal Properties

The thermal properties of the In-25.6Sn and In-35Sn were tested by a differential scanning calorimetry (DSC) machine (TA Discovery DSC 2500). Approximately $7 \pm 1 \text{ mg}$ small piece samples were sealed into Tzero aluminium pans and lids (Waters Australia Pty Ltd.) for measurement. Packed samples were heated from 20°C to 150°C, then cooled to 20°C under a ramp rate of 20°C/min, which is the same as the in situ heating SEM experiment. The nitrogen gas flow was set to 50 mL/

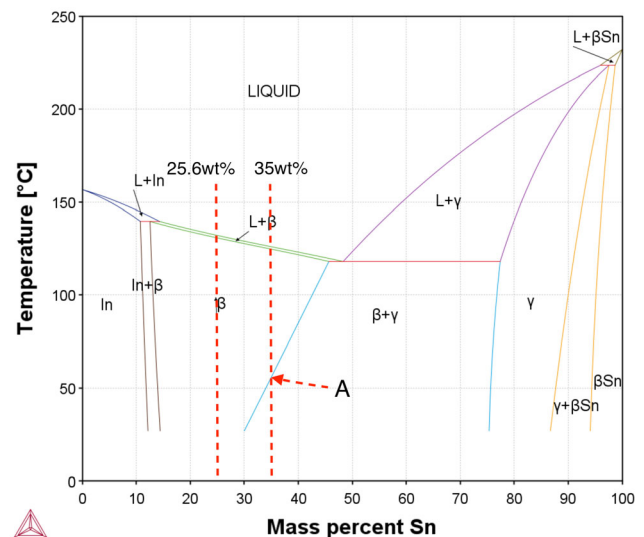


Fig. 1. In-Sn binary phase diagram calculated based on Thermo-calc 2022a²⁰ database (TCSLD4: Solder Alloy v4.1). Point A: the intersection of solvus line and In-35wt.%Sn at around 60°C.

min to protect the samples from oxidation. The testing was conducted twice for each composition to ensure repeatability.

In Situ Heating Microstructural Characterisation

The In-35Sn and In-25.6Sn samples were cast and remained at room temperature for 51 days and then cut into approximately 3*2*2 mm pieces with a surgical knife. An ion milling machine (Hitachi IM 4000 Plus Ion mill) was used to obtain a clean surface finish with each sample being ion milled for 16 min using 3 kV acceleration voltage, 1.5 kV discharge voltage and 3 mm eccentricity with a 30° ion beam irradiation angle and protected under a 0.11 mL/min argon gas flow. Samples were further cleaned by a plasma cleaner (Evacont 25 De-Contaminator RF Plasma Cleaning System) before analysis.

The microstructural analysis used an in situ heating scanning electron microscopy (SEM) (Hitachi SU3500-A) fitted with a Deben enhanced cool stage (- 25°C to + 160°C temperature range with a

calibrated $\pm 1^\circ\text{C}$ error). The videos and microstructure images of prepared samples were captured under variable pressure (VP) backscatter electron (BSE) mode at a 20-kV accelerating voltage with a 40-nm spot size. The energy dispersive X-ray spectroscopy (EDX) analysis for elemental analysis and X-ray mapping was carried out using an Oxford Xmax SDD EDX detector. For annealing experiments, an In-35Sn sample was heated to 90°C and held for 1 h to see the changes in microstructure and then cooled to room temperature. For melting experiments, In-25.6Sn and In-35Sn samples were heated to 140°C (above their melting points), held for 5 s and then directly cooled to room temperature. The ramp rate of the Deben stage was set to 20°C/min and EDX analysis was conducted immediately before heating and after cooling to capture the changes in composition. The temperature profiles are available in Video S1 and Video S2 in the supplementary material.

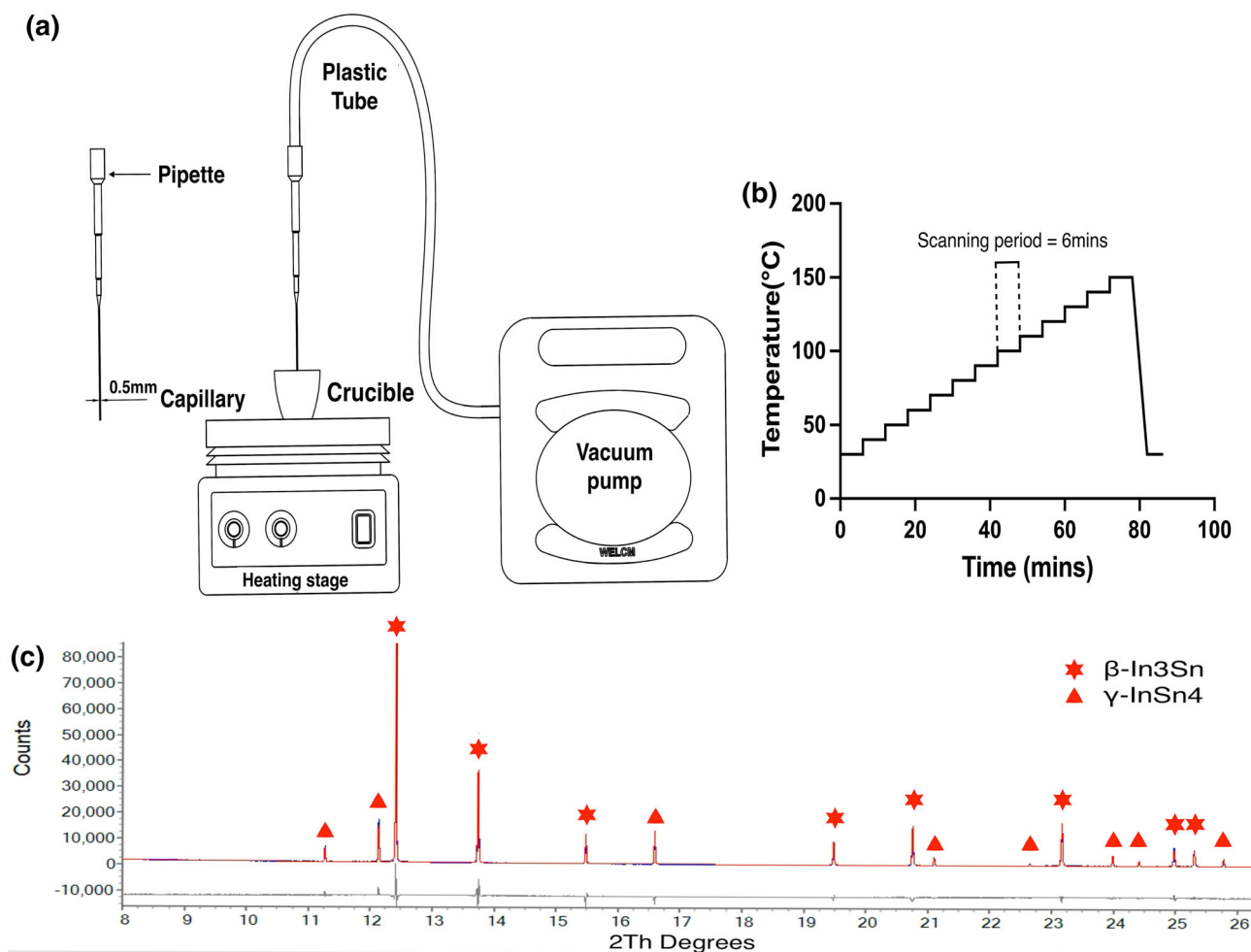


Fig. 2. (a) Schematic of PXRD sample preparation method; (b) temperature profile of in situ synchrotron PXRD experiment; (c) Rietveld refinement of the In-35Sn PXRD pattern at 30°C.

RESULTS AND DISCUSSION

Thermal Expansion Behaviour

Lattice Parameters in Crystal Structure

As shown in Fig. 3, because the β -In₃Sn and γ -InSn₄ have a body-centred tetragonal crystalline structure and hexagonal crystalline structure, respectively, here, the axis $a = b$ in the unit cell of both phases. There was a gradual rise in the lattice parameters of axis a and b as the temperature increased from 30°C to 130°C in Fig. 3a. Notably, the In-35Sn sample melted once the temperature reached 130°C; thus, the second and third scans at 130°C and measurements above this temperature were unavailable here. For the In-25.6Sn, as the temperature increases, the lattice parameters of all axes in β -In₃Sn increase. From the phase diagram in Fig. 1, no phase change is expected in this alloy suggesting temperature alone is the main factor responsible for this expansion of crystalline structure in In-25.6Sn. However, In-35Sn displays a more complex behaviour where the parameters of the c -axis in the β -In₃Sn unit cell exhibited a parabolic trend. Compared to the positive increasing trend of the a -axis there is a notable decrease in the c lattice parameter as the temperature increased from 30°C to 80°C, which is followed by an increasing trend as the temperature increased to

the melting point. This is evident in the PXRD patterns displayed in Fig. 8 where there is an increase in 2θ of β (002) at the beginning of heating, which is followed by a decrease (shifts to the left) as the temperature increases further. Contrarily, the 2θ of β (200) continuously shifts to the left during heating.

Comparing the lattice parameter curves of In-25.6Sn and In-35Sn in Fig. 3a and b shows that the lattice parameter of the a -axis in the β phase increases and the lattice parameter of the c -axis decreases accordingly at room temperature as the Sn content in the alloy increases. Therefore, the shrinking in lattice parameter of the c -axis in In-35Sn may be associated with the solubility of Sn in β -In₃Sn gradually increasing as the temperature increases from 30°C to 80°C, while the relative increase in a -axis may occur not only because of the thermal expansion but also the increase of Sn atoms in the lattice. This can be confirmed by the nonlinear curve in Fig. 3a, with the slope of the curve before 80°C being higher than the slope after 80°C. Moreover, notably, although the lattice parameter of the c -axis in the β -In₃Sn unit cell underwent a decrease with increasing temperature in the range of 30°C to 80°C, the cell volume of β -In₃Sn still increased (see Fig. 9). A 1.4% increase in the β cell volume of In-35Sn and a 0.9% increase in β cell volume of In-25.6Sn were detected during heating

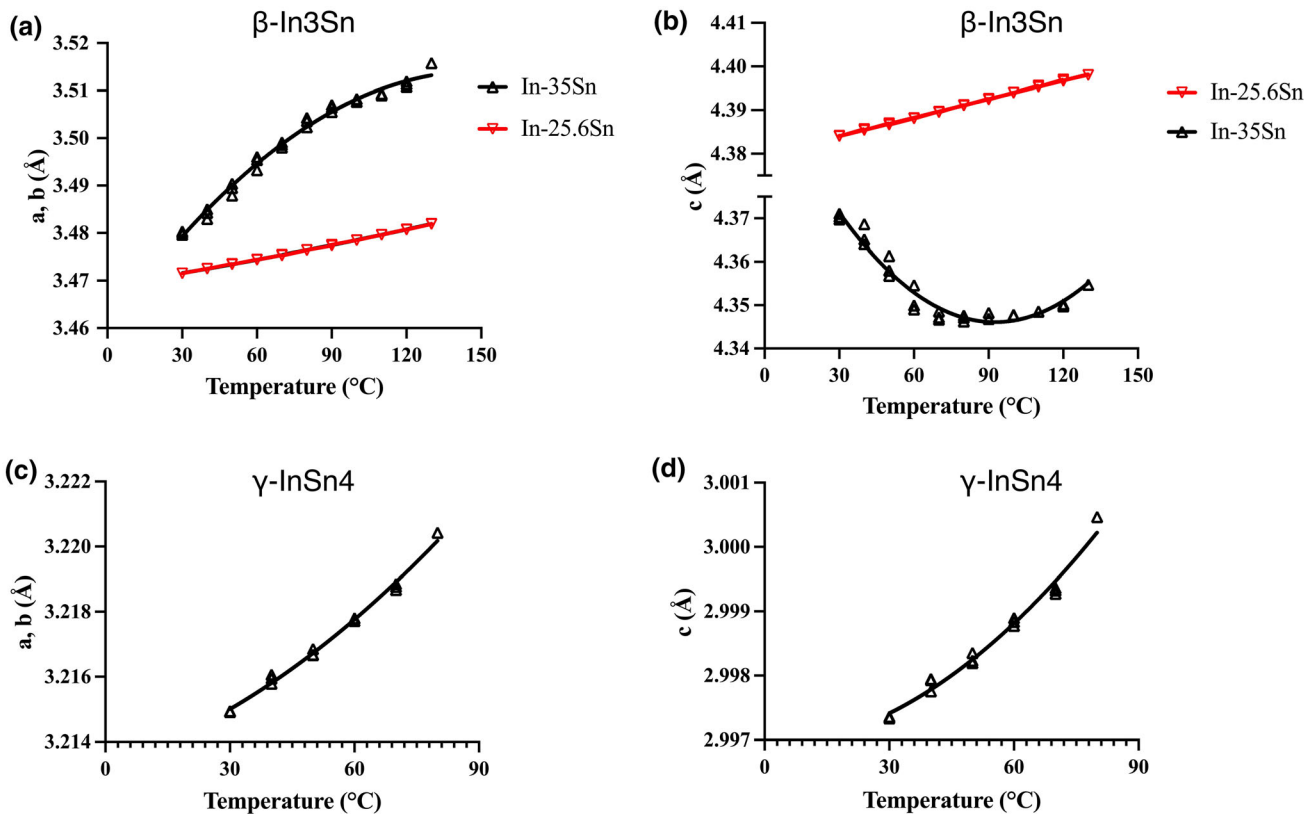


Fig. 3. Lattice parameters of phases in In-35Sn and In-25.6Sn. (a) a and b axes of the β -In₃Sn unit cell in In-35Sn and In-25.6Sn; (b) c -axis of the β -In₃Sn unit cell in In-35Sn and In-25.6Sn; (c) a and b axes of the γ -InSn₄ in In-35Sn; (d) c -axis of the γ -InSn₄ in In-35Sn.

from 30°C to 130°C; meanwhile, a 0.6% increase in γ cell volume of In-35Sn was detected when the temperature increased from 30°C to 80°C. In comparison, it has been reported that the β -Sn in Sn-3Ag-0.5Cu solder alloy had an approximately 1.2% volume expansion when it was heated from 30°C to its melting temperature.²¹

Compared to the β phase, the lattice parameters of the γ phase unit cell undergo a continual increase as the temperature rises and the phase starts becoming amorphous once the temperature reaches 80°C. Combined with the parabolic trend mentioned above, the phase transition happened when the temperature exceeded 80°C, and dissolution of the γ phase into the β phase caused the lattice parameter along the c -axis of the β phase to increase. In other words, the solubility of Sn in the β phase continuously increased when the temperature increased and crossed the solvus line (80°C) and reached the solubility limit when the temperature was 90°C, where only the β phase can be detected in the microstructure. At temperatures > 90°C, the concentration of Sn in In₃Sn remains constant. Thus, as the temperature increases further, the expansion of the crystalline structure occurs without any contribution from solute redistribution, similar to the β phase in In-25.6Sn. Therefore, for a given change in temperature, the solute redistribution between the two phases in In-35Sn, where applicable, appears to have a more significant effect on the change in lattice parameters. When referring to point A in the equilibrium phase diagram in Fig. 1, the intersection of In-35Sn on the solvus line is near

60°C, which is lower than the 80°C where a change in behaviour is apparent from the PXRD results. The relatively high ramp rate (30°C/min) and the reprecipitation of γ phase due to the oversaturation of Sn in β -In₃Sn are possible factors which may have contributed to this discrepancy.

CTE Determination

Figure 4 shows the CTE of the β and γ phases in In-35Sn and the β phase in In-25.6Sn calculated by the following equations:

$$dd_{hkl} = C_0 + C_1T + C_2T^2 \quad (1)$$

$$\alpha_{hkl} = \frac{C_1 + 2C_2T}{C_0 + C_1T + C_2T^2} \quad (2)$$

where T is the temperature and constants C_0, C_1, C_2 were fitted from lattice parameters with respect to temperature by a second order polynomial function. (Note: due to the difficulty of polynomial fitting for parabolic lattice parameter curve in In-35Sn, an uncertainty of magnitude of CTE needs to be considered here, though the trends are guaranteed.)

As shown in Fig. 4b and c, the CTE of the a -axis and c -axis in the γ phase of In-35Sn increase with the temperature, which shows a similar trend observed in the CTE of the β phase in In-25.6Sn. However, the CTE of In-35Sn shows an anisotropic thermal expansion behaviour especially for the β phase as the CTE along the c -axis increases with the temperature but CTE in the a -axis decreases

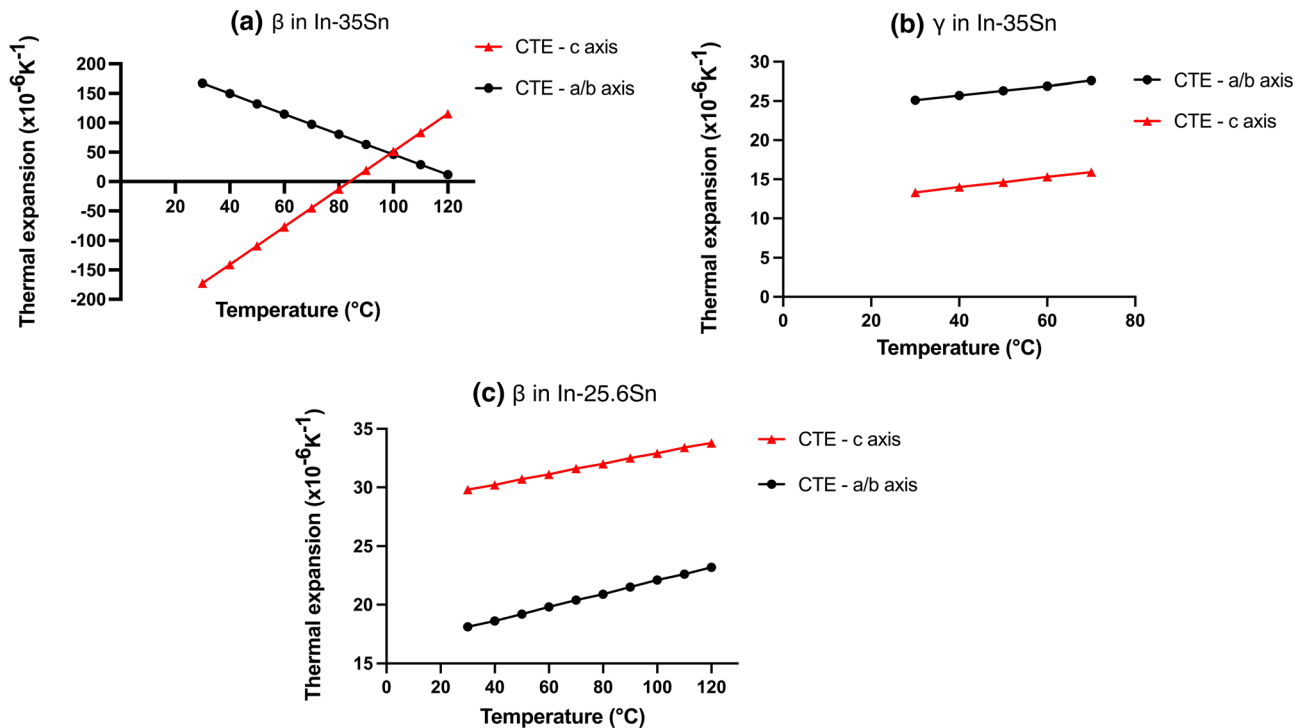


Fig. 4. Temperature dependence of the CTE in a, b and c directions for (a) β phase of In-35Sn; (b) γ phase of In-35Sn; (c) β phase of In-25.6Sn.

accordingly. The CTE along the c-axis transitioned from a negative value to a positive value when the temperature increased from room temperature to 80°C and above, indicating shrinking occurred while heating, matching the lattice parameter shown in Fig. 3. In comparison, the In-25.6Sn shows a much simpler thermal expansion behaviour, free from the complications of solute redistribution as the solubility of indium in the γ phase is relatively stable with temperature.

In Situ Heating SEM

Microstructure and Melting Characterisation

The DSC curves of In-25.6Sn and In-35Sn are shown in Fig. 5, and the peak analysis was carried out by the TA DSC software. The endothermic and exothermic peaks of In-35Sn are 125.9°C and 121.3°C, respectively, compared to the 132.8°C and 130.1°C for In-25.6Sn; peaks in In-35Sn show slightly lower temperatures compared to the result (126.7°C and 123.3°C for endothermic peak and exothermic peak, respectively) in our previous study¹⁶ as the ramp rate increased from 10 °C/min to 20 °C/min. Only one peak can be found on the DSC cooling curve for both compositions, which indicates that only the β phase was involved in solidification. Thus, it can be concluded that there is little difference between In-25.6Sn and In-35Sn in terms of solidification. However, at room temperature, the β phase in In-35Sn is supersaturated with Sn regarding the equilibrium phase diagram. The temperature gap between the exothermic and endothermic peaks is caused by non-equilibrium solidification and is minor for both compositions, being slightly larger for the In-35Sn alloy.

As shown in Fig. 6a and the EDX results in Fig. 7a, the γ phase in In-35Sn is generally shaped irregularly and shows an island-like morphology compared to the β phase in the background, and the grain size of the γ phase is variable. In comparison, In-25.6Sn shows a 100% β phase in the microstructure, and the EDX analysis supported a composition

of In₃Sn (see Fig. 10 and Table III). Clear grain boundaries of the β phase can be observed in both compositions, and the β -In₃Sn grains in In-25.6Sn are larger compared to those in In-35Sn.

The grain boundaries of the β phase were less apparent in In-35Sn when the temperature reached 129°C, which indicated the melting process was starting from the grain boundaries of the β phase (this can be observed in Video S1). The latency in heat transfer combined with the error (approximately $\pm 1^\circ\text{C}$) of the heating stage mean it is reasonable to expect such changes in microstructure may occur at a measured temperature slightly higher than the sample's melting point, which is 125.9°C, as shown in Fig. 5. The wrinkles on the liquid sample can be found in In-35Sn when the temperature was further increased to 140°C; these patterns in microstructure were caused by a solid oxide film as it has been reported that In-Sn alloys easily suffer from oxidation.²² Despite the dissolution of the γ phase being confirmed by XRD the phase boundaries between the β and γ phase appeared to persist during variable temperature SEM. In comparison, In-25.6Sn exhibited a clearer melted morphology when the temperature went above its melting point (132.8°C) and no changes with further heating to 140°C were observed.

The In-25.6Sn shows a globular structure compared to the more branched dendritic structure in In-35Sn, which indicates the constitutional undercooling increased with the increased solute concentration.²² The stability of a solid-liquid interface shape relates to G/V , and the observation here can be verified as shown in Eq. 4:^{23,24}

$$\frac{G}{V} = \frac{mC_0}{D} \left\{ \frac{1-k}{k} \right\} \quad (3)$$

where G is the temperature gradient, V is the solidification velocity, m is the slope of the liquidus line, C_0 is the original melt composition, D is the diffusion coefficient of solute in the liquid and k is the segregation coefficient. From the equilibrium phase diagram, m for In-35Sn is a negative value

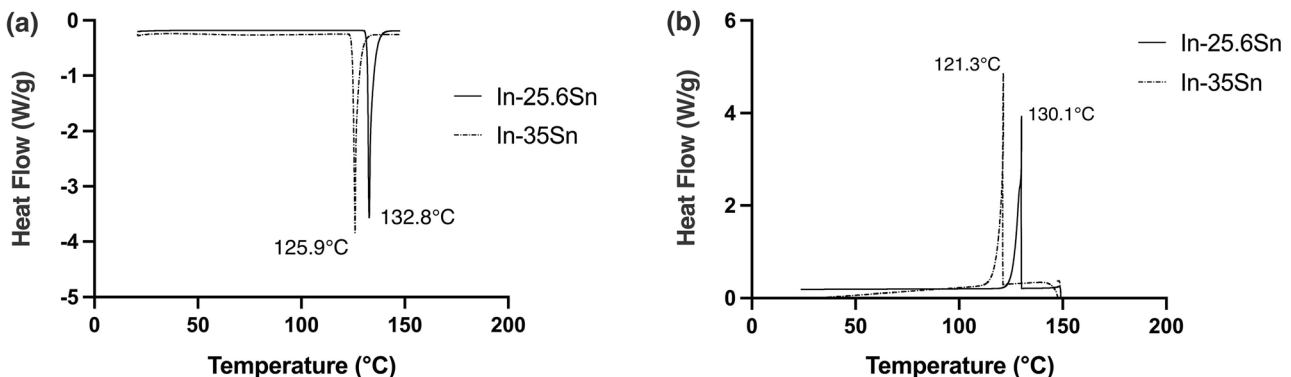


Fig. 5. DSC curves of tested samples. (a) Heating curves with endothermic peaks; (b) cooling curves with exothermic peaks.

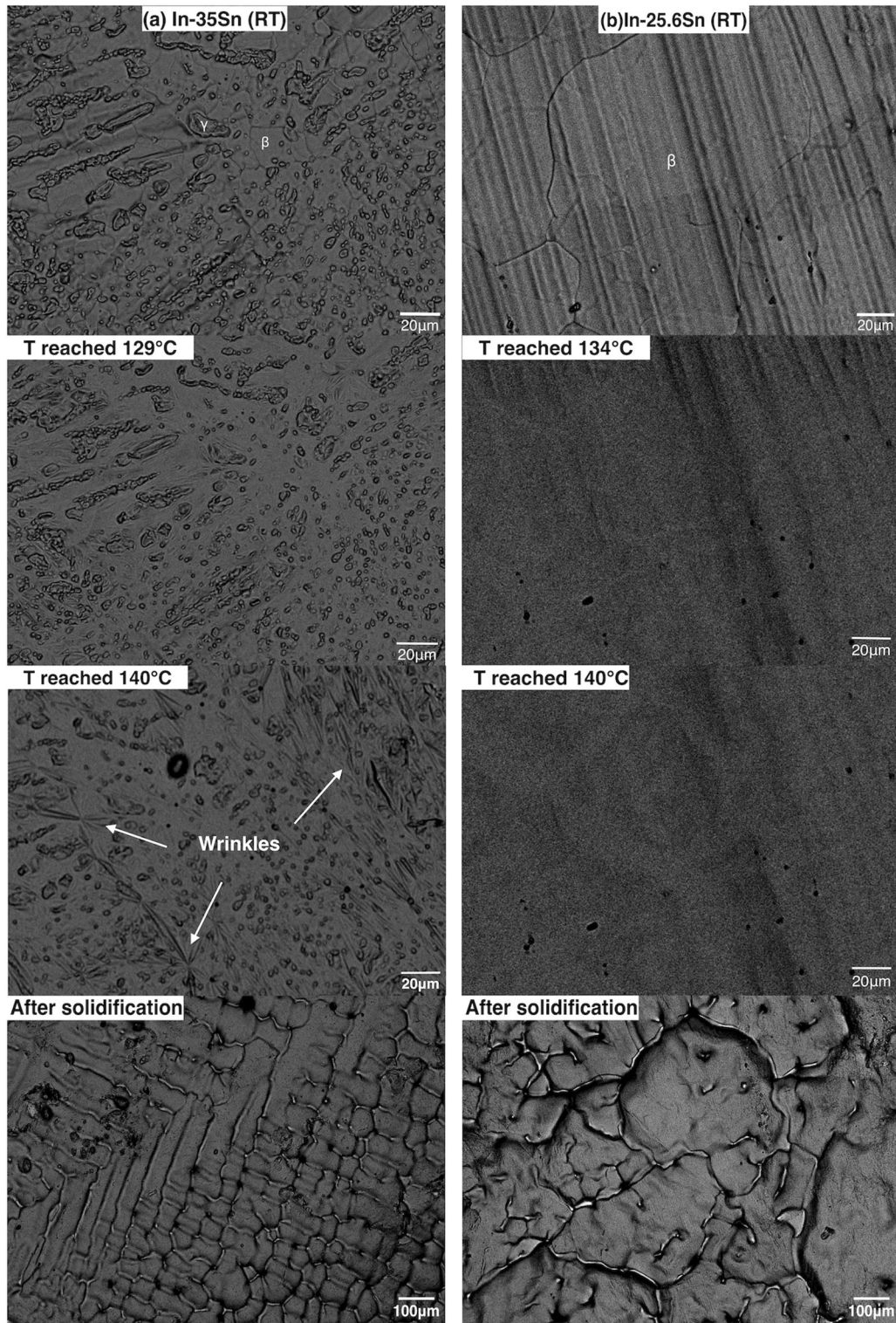


Fig. 6. Microstructure before/after melting and solidification during SEM observation of (a) In-35Sn; (b) In-25.6Sn.

and expected to be close to m for In-25.6Sn; the value of k was calculated to be in the range of 0.92–0.94 for both alloys approximately and assuming that the diffusion coefficient in this system is consistent, the equation can be simplified to

$$\frac{G}{V} = -A * C_0 \quad (4)$$

Thus, In-35Sn has a higher critical G/V compared to the In-25.6Sn, which means for equivalent

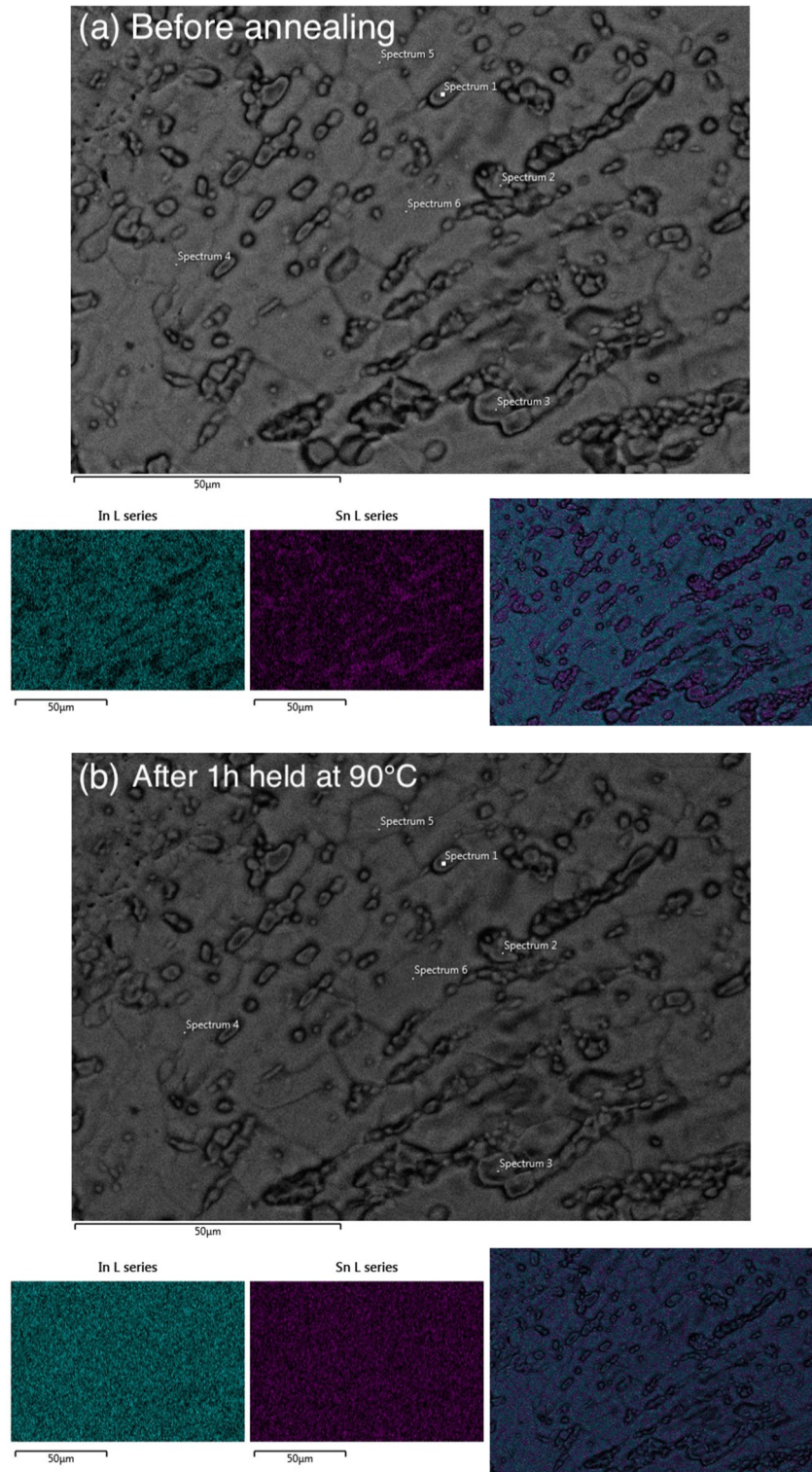


Fig. 7. Microstructure and EDX mapping of In-35Sn. (a) Before annealing; (b) after 1 h holding at 90°C. The EDX spectrum analysis is summarised in Table I.

cooling conditions the more dendritic structure is expected in In-35Sn, consistent with the growth morphology observed by the synchrotron in situ PXRD previously.²⁵ Due to the shallow slope of the liquidus (low absolute value of m) and close spacing

between solidus and liquidus line in equilibrium phase diagram in Fig. 1 (partition coefficient k close to 1) segregation occurs largely due to the high amount of solute present rather than a strong tendency for constitutional undercooling. This

Table I. EDX spectrum analysis for element weight proportion in In-35Sn before and after annealing

Spectrum	In (wt.%) _{before}	Sn (wt.%) _{before}	In (wt.%) _{after}	Sn (wt.%) _{after}
1	31.6	68.4	65.2	34.8
2	31.2	68.8	59.9	40.1
3	30.9	69.1	64.8	35.2
4	70.6	29.4	65.5	34.5
5	70.4	29.6	65.4	34.6
6	70.3	29.7	64.6	35.4

Table II. EDX spectrum analysis for element weight proportion in In-35Sn (7 days after annealing)

Spectrum	In (wt.%) _{7 days}	Sn (wt.%) _{7 days}
1	70.5	29.5
2	38.5	61.5
3	70.0	30.0
4	69.6	30.4
5	61.9	38.1
6	64.0	36.0

segregation is apparent as an interdendritic segregation of eutectic phases while considering the lower diffusion energy in the system which caused the lack of eutectic solidification peak in the DSC analysis (see Fig. 6a).

Annealing Effect

By comparing the EDX maps in Fig. 7a and b, the dissolution of γ phase happened after 1 h annealing with almost no obvious morphological changes in microstructure (i.e., the island-like grain boundaries remain). Notably, the EDX analysis in this work was conducted immediately after the sample was cooled to the room temperature. From the EDX analysis displayed in Table I, all spectra present as indium-rich phases after annealing, while compared to the β phase (spectra 4, 5 and 6 before annealing), there is an obvious increase in Sn content which proved that the solute redistribution has caused γ phase to transform into β phase, which dominates the microstructure when the temperature goes above 80°C, and this observation matches the PXR data discussed above.

The annealed sample was placed at room temperature for 7 days to evaluate the reprecipitation behaviour of the γ phase. The microstructure and EDX mapping of the In-35Sn sample (7 days after annealing) are shown in Fig. 11 in the Appendix and the detailed atomic concentration is summarised in Table II. The γ phase starts reprecipitating randomly in the microstructure from the oversaturated beta phase, the EDX mapping of Sn L series shows a different high Sn concentration area from those in Fig. 7a, and again, the morphology of

the initial γ grains remains the same. Only spectrum 2 shows a Sn-rich phase while the Sn atomic concentration in spectra 1, 3 and 4 decreases, which indicates the reprecipitation of γ phase has occurred. Compared to the atomic concentration after annealing at 90°C, spectra 5 and 6 still exhibit an oversaturated β phase, which indicates that the reprecipitation of γ phase is a time-consuming process and the supersaturation of Sn in β phase only decreases slowly with time at room temperature.

CONCLUSION

The solidification and temperature-dependant microstructure stability and crystallography of two different Sn-In alloys were examined using a range of experiments. A real-time annealing experiment based on the PXR results has been conducted to simulate the real solder working condition in electronic devices.

- The In-35Sn was shown to have a different thermal expansion behaviour compared to the In-25.6 because of the dissolution of the γ phase in the microstructure. The solubility of Sn in the β phase was confirmed to be temperature sensitive and at the rate of heating used in the experiments, 80°C was a critical temperature for complete dissolution of γ in In-35Sn. The c-axis in the β phase of In-35Sn shows a negative thermal expansion (NTE) from 30°C to 80°C and shrinks during heating, which may be associated with benefits as a solder alloy for temperature-sensitive applications. In comparison, the lattice parameters of In-25.6Sn show a simpler expansion when heating in this temperature range.
- In situ heating SEM showed a more dendritic structure in In-35Sn after solidification compared to the more globular structure in In-25.6Sn. The experiment also verified the dissolution of γ phase happened after 1 h of annealing at 90°C and γ dissolved into the β phase. Furthermore, when the temperature crosses the solvus line under relatively high cooling rates, there is a propensity for the β phase to become supersaturated with Sn atoms.
- The reprecipitation of the γ phase to equilibrium levels is a slow process at room temperature.

Such changes in phase composition and proportions will be of significance in Sn-In alloys as the γ phase is of importance in the mechanical properties of In-Sn alloys.¹⁶ Therefore, the In-Sn alloys may be more suitable for lower temperature applications (operating below 80°C) and further development is required to take full advantage of the NTE property in the c-axis of the β phase. It may also be possible to stabilise the microstructure through modifications to the composition and inclusion of additional elements.

SUPPLEMENTARY INFORMATION

The online version contains supplementary material available at <https://doi.org/10.1007/s11837-023-05870-y>.

ACKNOWLEDGEMENTS

We acknowledge (1) the Centre for Microscopy and Microanalysis at The University of Queensland for providing the ion-milling machine, plasma cleaner and in situ heating stage compatible SEM; (2) Nihon Superior Company Ltd. for their support of this research and the supply of the indium ingots; (3) translational polymer research group team and Dr. Clement Chan for providing the DSC instrument; (4) Dr. Tony Wang (from Queensland University of Technology's Central Analytical Research Facility) for helping with the TOPAS Rietveld Refinement; (5) Powder Diffraction beamline at the Australian Synchrotron for the synchrotron PXRD experiments.

FUNDING

Open Access funding enabled and organized by CAUL and its Member Institutions. This research was funded by the Australian Research Council (ARC), Australia (LP180100595) and The Uni-

versity of Queensland, Australia, (Research Training Program) stipend and (Knowledge Exchange & Translation Fund, 2021002690). The synchrotron PXRD data was collected at the Australian Synchrotron Powder Diffraction beamline under proposal (AS221/PD/17948).

CONFLICT OF INTEREST

The authors declare that they have no conflict of interest.

OPEN ACCESS

This article is licensed under a Creative Commons Attribution 4.0 International License, which permits use, sharing, adaptation, distribution and reproduction in any medium or format, as long as you give appropriate credit to the original author(s) and the source, provide a link to the Creative Commons licence, and indicate if changes were made. The images or other third party material in this article are included in the article's Creative Commons licence, unless indicated otherwise in a credit line to the material. If material is not included in the article's Creative Commons licence and your intended use is not permitted by statutory regulation or exceeds the permitted use, you will need to obtain permission directly from the copyright holder. To view a copy of this licence, visit <http://creativecommons.org/licenses/by/4.0/>.

APPENDIX

See Figs. 8, 9, 10, 11 and Table III.

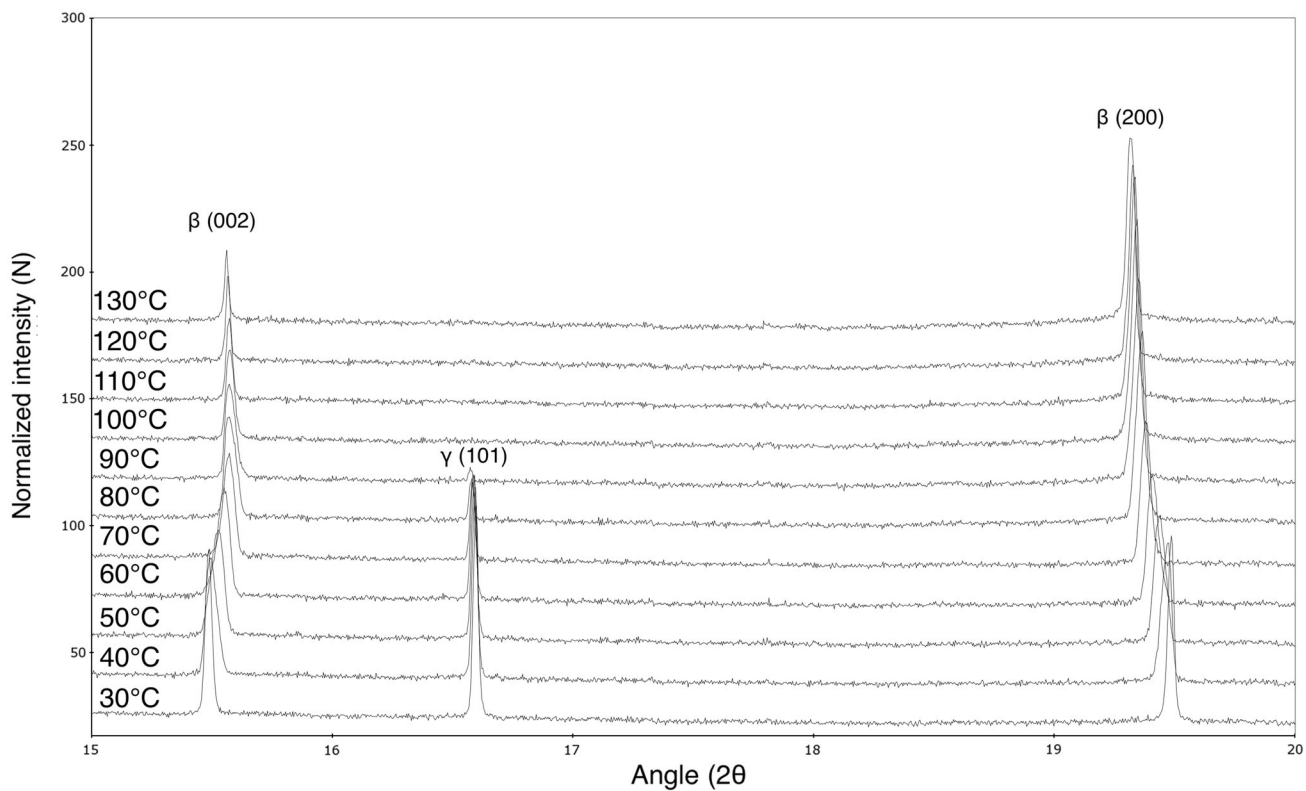


Fig. 8. Synchrotron PXRD patterns of In-35Sn between 2θ of 15–20.

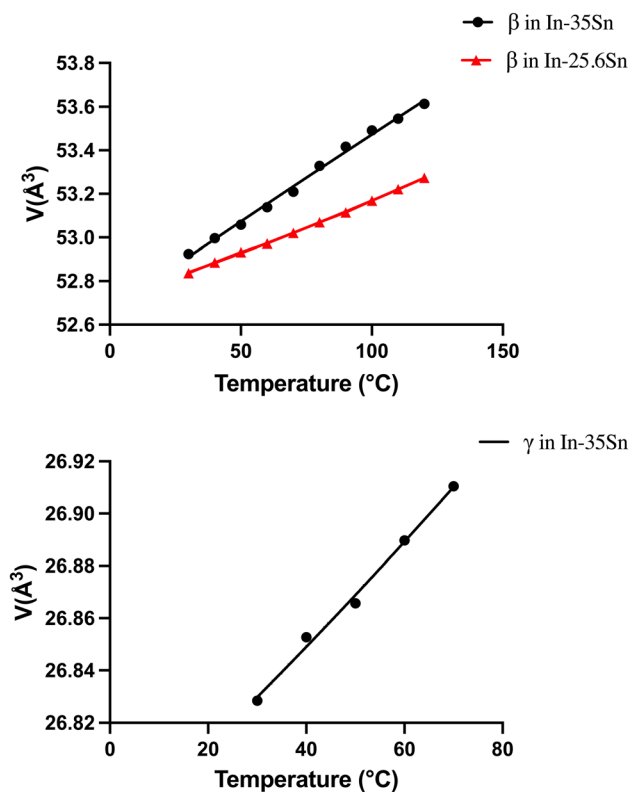


Fig. 9. Volume expansion with temperature in unit cell.

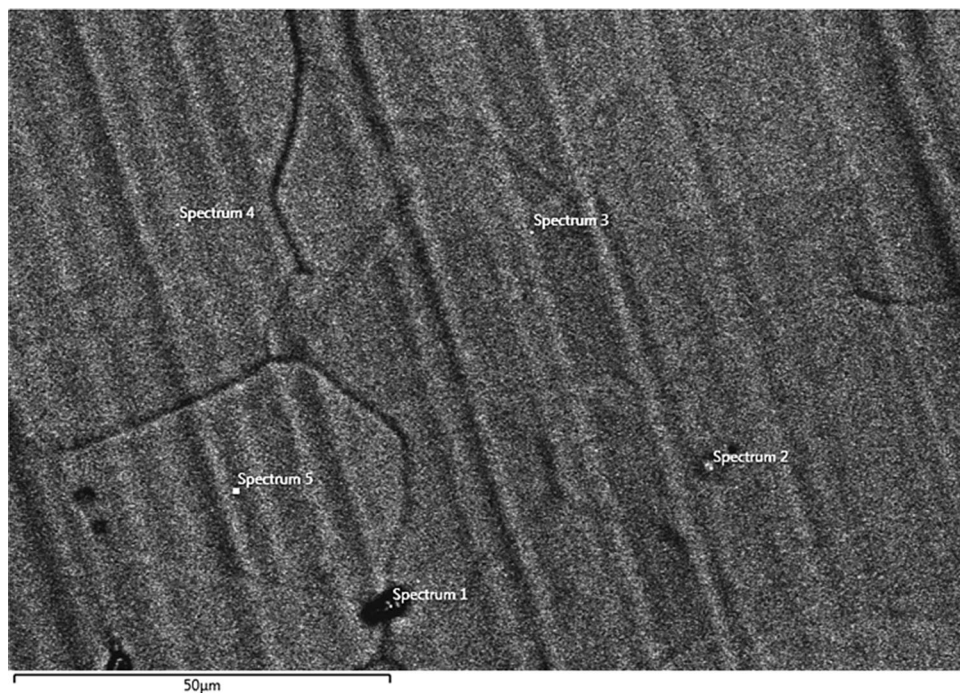


Fig. 10. Microstructure of In-25.6Sn with spectra analysed by EDX.

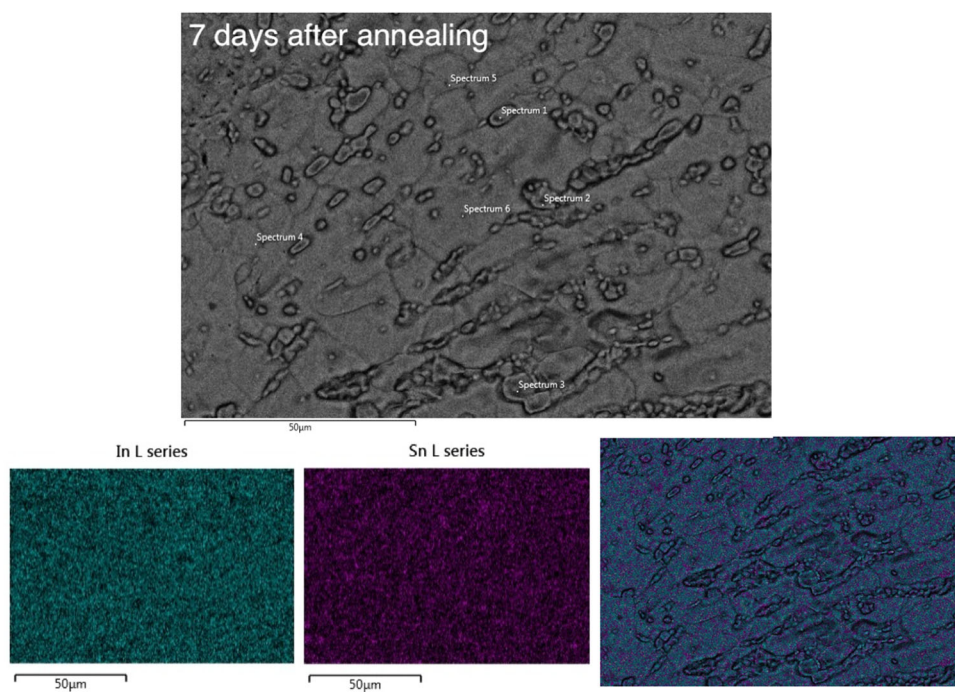


Fig. 11. Microstructure and EDX mappings of In-35Sn 7 days after annealing experiment.

Table III. EDX spectrum analysis for element weight proportion in In-25.6Sn at room temperature

Spectrum	In (wt.%)	Sn (wt.%)	Cu (wt.%)	Ni (wt.%)
1	65.1	28.6	4.1	2.2
2	76.3	23.7	–	–
3	75.7	24.3	–	–
4	76.0	24.0	–	–
5	74.8	25.2	–	–
6	75.8	24.2	–	–

REFERENCES

- Ahmed S, Basit M, Suhling JC, P. Lall. 2016 15th IEEE intersociety conference on thermal and thermomechanical phenomena in electronic systems (ITherm), 746–754 (2016).
- J. Zhang, Z. Hai, S. Thirugnanasambandam, J.L. Evans, M. Bozack, R. Sesek, Y. Zhang, and J.C. Suhling, *SMTA J.* 25, 19 (2012).
- J.A. Depiver, S. Mallik, and D. Harmanto, *Adv. Mater. Process. Technol.* 7, 1 <https://doi.org/10.1080/2374068X.2020.1751514> (2021).
- E. Dalton, G. Ren, J. Punch, and M.N. Collins, *Mater. Des.* 154, 184 <https://doi.org/10.1016/j.matdes.2018.05.030> (2018).
- M.-C. Liao, P.-S. Huang, Y.-H. Lin, M.-Y. Tsai, C.-Y. Huang, and T.-C. Huang, *Appl. Sci.* 7, 739 (2017).
- Q. Hao, X.F. Tan, Q. Gu, K. Sweatman, S.D. McDonald, and K. Nogita, *JOM* 74, 1739 <https://doi.org/10.1007/s11837-021-05145-4> (2022).
- H. Xu, T.K. Lee and C.U. Kim. 2014 IEEE 64th electronic components and technology conference (ECTC), 133–138 (2014).
- R. Tian, C. Hang, Y. Tian, and L. Zhao, *Mater. Sci. Eng. A* 709, 125 <https://doi.org/10.1016/j.msea.2017.10.007> (2018).
- J.W. Nah, F. Ren, K.N. Tu, S. Venk, and G. Camara, *J. Appl. Phys.* <https://doi.org/10.1063/1.2163982> (2006).
- F. Gnecco, E. Ricci, S. Amore, D. Giuranno, G. Borzone, G. Zanicchi, and R. Novakovic, *Int. J. Adhes Adhes.* 27, 409 <https://doi.org/10.1016/j.ijadhadh.2006.09.008> (2007).
- M. Deshpande, R. Chaudhari, P.R. Narayanan, and H. Kale, *J. Mater. Eng. Perform.* 30, 7958 <https://doi.org/10.1007/s11665-021-05983-y> (2021).
- M. Plötner, B. Donat, and A. Benke, *Cryogenics (Guildford)* 31, 159 [https://doi.org/10.1016/0011-2275\(91\)90169-W](https://doi.org/10.1016/0011-2275(91)90169-W) (1991).
- R.W. Chang, and F.P. McCluskey, *Cryogenics (Guildford)* 49, 630 <https://doi.org/10.1016/j.cryogenics.2009.02.003> (2009).
- J.H. Wernick, and B.T. Matthias, *J. Chem. Phys.* 34, 2194 <https://doi.org/10.1063/1.1731856> (1961).
- T. Mousavi, C. Aksoy, C.R.M. Grovenor, and S.C. Speller, *Supercond. Sci. Technol.* 29, 15012 <https://doi.org/10.1088/0953-2048/29/1/015012> (2015).
- J. Zhou, X.F. Tan, S.D. McDonald, and K. Nogita, *Materials.* <https://doi.org/10.3390/ma15238321> (2022).
- V.T. Deshpande, and D.B. Sirdeshmukh, *Acta Cryst.* 14, 355 <https://doi.org/10.1107/S0365110X61001212> (1961).
- A. Pietriková, J. Bednarcik, and J. Durišin, *J. Alloy. Compd.* 509, 1550 <https://doi.org/10.1016/j.jallcom.2010.09.153> (2011).
- M. Branch Kelly, A. Kirubanandham, and N. Chawla, *Mater. Sci. Eng. A* 771, 138614 (2020).
- J.O. Andersson, T. Helander, L. Höglund, P. Shi, and B. Sundman, *Calphad* 26, 273 [https://doi.org/10.1016/S0364-5916\(02\)00037-8](https://doi.org/10.1016/S0364-5916(02)00037-8) (2002).
- A. Pietriková, J. Bednarcik, and J. Durisin, *J. Alloy. Compd.* 509, 1550 <https://doi.org/10.1016/j.jallcom.2010.09.153> (2011).
- J. Kim, H. Schoeller, J. Cho, and S. Park, *J. Electron. Mater.* 37, 483 <https://doi.org/10.1007/s11664-007-0346-7> (2008).
- J. Campbell, *Complete casting handbook* (Elsevier Science & Technology, Oxford, 2015), pp187–253.
- L.M. Hogan†, (Elsevier Ltd, 2011), pp 1913–1918.
- M.S. Chang, M.A.A.M. Salleh, D.S.C. Halin, M.I.I. Ramli, H. Yasuda, and K. Nogita, *J. Alloys Compd.* 897, 163172 <https://doi.org/10.1016/j.jallcom.2021.163172> (2022).

Publisher's Note Springer Nature remains neutral with regard to jurisdictional claims in published maps and institutional affiliations.